Natural Hazards
and Earth System
Sciences

Open Access

# Distributions of nonlinear wave amplitudes and heights from laboratory generated following and crossing bimodal seas

**P. G. Petrova and C. Guedes Soares**

Centre for Marine Technology and Engineering (CENTEC), Instituto Superior Técnico, Universidade de Lisboa, 1049-001 Lisbon, Portugal

*Correspondence to:* C. Guedes Soares (c.guedes.soares@centec.tecnico.ulisboa.pt)

**Abstract.** This paper presents an analysis of the distributions of nonlinear crests, troughs and heights of deep water waves from mixed following sea states generated mechanically in an offshore basin and compares with previous results for mixed crossing seas from the same experiment. The random signals at the wavemaker in both types of mixed seas are characterized by bimodal spectra following the model of Guedes Soares (1984). In agreement with the Benjamin–Feir mechanism, the high-frequency spectrum shows a decrease in the peak magnitude and downshift of the peak with the distance, as well as reduction of the tail. The observed statistics and probabilistic distributions exhibit, in general, increasing effects of third-order nonlinearity with the distance from the wavemaker. However, this effect is less pronounced in the wave systems with two following wave trains than in the crossing seas, given that they have identical initial characteristics of the bimodal spectra. The relevance of third-order effects due to free modes only is demonstrated and assessed by excluding the vertically asymmetric distortions induced by bound wave effects of second and third order. The fact that for records characterized by relatively large coefficient of kurtosis, the empirical distributions for the non-skewed profiles continue deviating from the linear predictions, corroborate the relevance of free wave interactions and thus the need of using higher-order models for the description of wave data.

## 1 Introduction

Much interest has been recently directed towards understanding of the observed extreme waves with relatively low probabilities of occurrence in view of their effect on ships (Guedes Soares et al., 2008) and offshore structures (Fonseca et al., 2010). In this respect, controlled model tests in a laboratory are useful in studying the characteristics of waves that rarely occur at sea and the corresponding responses of marine structures, which can be used to validate the codes for calculating ship responses. Analyses of oceanic data collected in stormy seas seem to indicate the validity of linear models for the distributions of large wave heights (Tayfun and Fedele, 2007; Casas-Prat and Holthuijsen, 2010), and of second-order models for wave crests and troughs (Tayfun, 2006, 2008). However, deviations between the theoretical predictions and the observations do occur at low probability levels when the measurements contain relatively rare, exceptionally large waves, referred to as abnormal, rogue or freak waves (Petrova et al., 2007).

Thorough description of different aspects of the so-called abnormal waves is provided by Kharif et al. (2009). One of the likely mechanisms for abnormal wave occurrence is the Benjamin–Feir instability due to third-order quasi-resonant interactions between free waves when the initial spectra represent narrowband long-crested conditions (Onorato et al., 2001; Janssen, 2003; Onorato et al., 2004; Onorato and Proment, 2011). The likelihood of this mechanism is quantified by the Benjamin–Feir index (BFI) of Janssen (2003) (see also Onorato et al., 2001). Favourable conditions for instability can be generated mechanically in wave tanks (Onorato et al., 2004; Waseda et al., 2009; Cherneva et al., 2009; Shemer and Sergeeva, 2009), or can be simulated numeri-

cally (Onorato et al., 2001; Mori and Yasuda, 2002; Socquet-Juglard et al., 2005; Toffoli et al., 2008, Zhang et al., 2013). Onorato et al. (2004) provided the first experimental evidence that the nonlinear wave statistics depends on BFI. However, the initial requirements for instability make this mechanism unlikely to be the primary cause for the majority of extreme wave occurrences in oceanic conditions, characterized by broader spectra and directional spread (Forristall, 2007, Guedes Soares et al., 2011). Numerical studies (Onorato et al., 2002; Socquet-Juglard et al., 2005; Gramstad and Trulsen, 2007) and laboratory experiments (Onorato et al., 2009; Waseda et al., 2009) analysing the effect of directionality show that the wave train becomes increasingly unstable towards long-crested conditions.

The superposition of two wave systems propagating in different directions could explain some cases of rogue wave occurrences. Such extreme conditions at sea are reported in relation to accidents and worsened operability of ships and offshore platforms in heavy weather (Guedes Soares et al., 2001; Toffoli et al., 2005). Onorato et al. (2006a) proposed a system of two coupled nonlinear Schrödinger equations (CNLS) to explain the formation of wave extremes in crossing seas (see also Shukla et al., 2006), showing that the second wave train advancing at a certain critical angle facilitates the modulational instability. These findings are validated by numerical simulations of the Euler equations, as well as by laboratory experiments (Onorato et al., 2010; Toffoli et al., 2011). It has also been found that the coefficient of kurtosis increases up to 40° of crossing between the wave trains and then stabilizes, reaching a maximum between 40 and 60°.

A hindcast approach is used to explain recent cases of extremely large waves. Tamura et al. (2009) demonstrated that the wind–sea energy of a studied complex wave field contributed to the exponential growth of the swell system, generating a unimodal "freakish" sea. Cavaleri et al. (2012) analysed the sea state conditions at the time of the accident with the Louis Majesty cruiser characterized by the coexistence of two wave systems of comparable energies and peak periods, propagating at 40–60°. Furthermore, the possible rogue wave conditions at the time of the accident have been successfully, though qualitatively, modelled using a system of two coupled nonlinear Shrödinger equations.

The statistical analysis of wave data usually addresses sea states represented by single-peaked spectra, though the oceanic sea states are more complex (Guedes Soares, 1991), in the sense of being described by two-peaked spectra (Guedes Soares, 1984), or by more complex spectra (Boukhanovski and Guedes Soares, 2009). The probability distributions of wave heights in such sea states have been studied within the linear theory by Rodríguez et al. (2002) for numerically simulated data, and by Guedes Soares and Carvalho (2003, 2012) for oceanic data. The Rayleigh distribution was found to systematically overestimate the observations and fit the data only in the case of wind-dominated sea states with low intermodal distances. The approximation

of Tayfun (1990) was suitable only for wind–sea dominated wave fields with large and mainly moderate intermodal distances.

The effect of combined seas on the wave crest statistics, surface elevation skewness and kurtosis was shown for the first time by Bitner-Gregersen and Hagen (2003) for second-order time domain simulations. Higher wave crests and larger nonlinear statistics have been reported for wind-dominated seas. Arena and Guedes Soares (2009) performed Monte Carlo simulations of second-order waves with bimodal spectra representative of the Atlantic Ocean. They reported good agreement between the empirical wave height distributions and the linear model of Boccotti (1989, 2000), as well as between the distributions of nonlinear wave crests/troughs and the second-order formulation of Fedele and Arena (2005). Petrova et al. (2013) presented results on the contribution of third-order nonlinearity to the wave statistics both in terms of the angle of incidence between the two crossing wave systems and the evolution of waves along the tank. Though those results are not conclusive, it was possible to observe various effects of third-order nonlinearity which, in general, become stronger down the basin and especially at the last four gauges. The distributions of wave crests and troughs for a large angle of crossing are more likely to be predicted by the weakly nonlinear narrowband models.

Following the lines above, the present work provides further analysis of the behaviour of laboratory-generated irregular mixed seas. In particular, the work concentrates on the wave statistics and probabilistic distributions observed for combined seas with two following wave systems and makes a comparison with some results for two obliquely propagating wave systems (Petrova et al., 2013). The study aims at assessing and analysing the third-order effects on the nonlinear statistics in the presence of a second wave component in terms of the propagated distance along the basin. The behaviour of the nonlinear statistics indicating increased probability of abnormal waves is associated here with a possible Benjamin–Feir instability. Such instability can be expected in the high-frequency range of the bimodal spectra, due to the large initial steepness–bandwidth ratios.
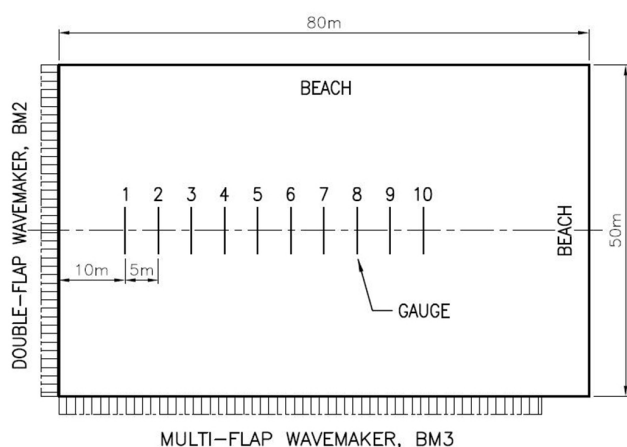
## 2 Laboratory data: basic spectral and statistical parameters

The set of laboratory data, representative of following and crossing seas, originates from an experiment carried out in the Marintek offshore basin, Trondheim, Norway. The basin has 80 m length, 50 m width and an adjustable bottom set to 2 m (Fig. 1).

The BM2 double-flap wavemaker and the BM3 multi-flap wavemaker were operating depending on the type of the sea state being generated: mixed sea with two wave systems advancing in the same direction (following sea) or mixed sea with two wave systems crossing at an angle (crossing sea)

**Table 1.** Target characteristics of the mechanically generated bimodal sea states.

| Mixed seas | Test | $H_s$ (m) | $T_p$ (s) | Spectrum | Wave dir $\theta$ (°) | Wavemaker |
|---|---|---|---|---|---|---|
| Following | 8228 | 4.6/2.3 | 7/14 | 2P J3/J3 | 0/0 | BM2 |
| | 8229 | 4.6/2.3 | 7/20 | 2P J3/J3 | 0/0 | BM2 |
| | 8230 | 3.6/3.6 | 7/14 | 2P J3/J3 | 0/0 | BM2 |
| | 8231 | 3.6/3.6 | 7/20 | 2P J3/J3 | 0/0 | BM2 |
| Crossing | 8233 | 3.6/3.6 | 7/20 | 2P J3/J3 | 0/60 | BM2/BM3 |
| | 8234 | 3.6/3.6 | 7/20 | 2P J3/J3 | 0/120 | BM2/BM3 |
| | 8235 | 3.6/3.6 | 7/20 | 2P J3/J3 | 0/90 | BM2/BM3 |



**Figure 1.** Sketch of the ocean basin facility and test equipment at Marintek.

(see Table 1 for details). In the former case, both wave systems were generated by the BM2 double-flap wavemaker. The bimodal crossing seas, on the other hand, were generated by both wavemakers operating simultaneously: BM2 for the high-frequency modes and the multiflap wavemaker BM3 for the low-frequency modes. The problems with wave reflection and rise of water level along the basin were resolved by placing wave energy absorbing beaches at the two walls across each wavemaker. The instantaneous surface elevations were measured simultaneously by the set of ten gauges uniformly deployed at 5 m distance between each other along the midline of the basin; the distance between the first gauge and BM2 was set at 10 m (Fig. 1).

The laboratory experiment was run in model scale 1 : 50. However, it must be noted that all analyses and comparisons in this study are based on full-scale data, which brings a better understanding of the properties of the sea states generated during the experiment.

The conditions at the wavemaker provided random realizations described by the two-peaked spectral formulation of Guedes Soares (1984), so that the individual spectral components have JONSWAP shape with peak enhancement factor $\gamma = 3$ (J3), significant wave heights in combinations of

4.6/2.3 m and 3.6/3.6 m and full-scale peak periods in combinations of 7/20 s or 7/14 s (see the corresponding columns in Table 1). The individual JONSWAP spectra describe long-crested waves propagating at a certain angle with respect to the axis along the basin, such as $\theta = 0°$ describes a wave system propagating parallel to that axis. The angles of propagation for the crossing wave systems are: $\theta = 60, 90$ and $120°$ (Table 1). Each realization of the sea surface elevations is based on the random amplitude/phase model.

The full-scale total duration of the time series exceeds 3 h, given that the records are digitally sampled at uniform intervals, $dt = 0.1768$ s. The initial transient waves were removed by performing a truncation at the beginning of each record. The number of ordinates to be truncated was estimated depending on the time that the harmonic with twice the higher peak frequency takes to reach the last gauge in the tank. The length of the time series at the last gauge was used as a reference to cut the other records, so that finally for each test run one obtains a set of 10 records of equal length of approximately 3 h duration each. The 3 h record contains about 1400 waves which are expected to provide convergence of the probabilistic distributions at the low probability levels. The experimental conditions define the waves as propagating in deep water of constant depth, $d = 100$ m (linear scale 1 : 50). However, the deep water condition can be verified only for the short waves, while the long waves behave as propagating in intermediate water depth.

Table 2 provides the parameters characterizing the individual JONSWAP components: significant wave height, $H_s = 4\sigma$, $\sigma$ = standard deviation of the sea surface elevations; sea state steepness, $\varepsilon = k_p\sigma$, where $k_p$ = wave number at the peak frequency $\omega_p$; spectral width, represented by $\Delta$ = half width at half of the spectral maximum. The last column in the table quantifies the instability in the random field in terms of the Benjamin–Feir index (BFI), as defined by Janssen (2003)

$$\text{BFI} = \frac{\varepsilon\sqrt{2}}{\Delta\omega/\omega_p} \qquad (1)$$

such as the random wave train is unstable when $\text{BFI} > 1$. Onorato et al. (2004) provided for the first time an experimental proof for the existing connection between the large

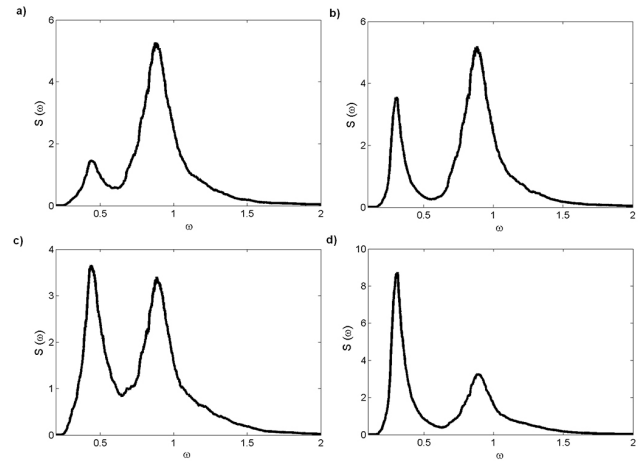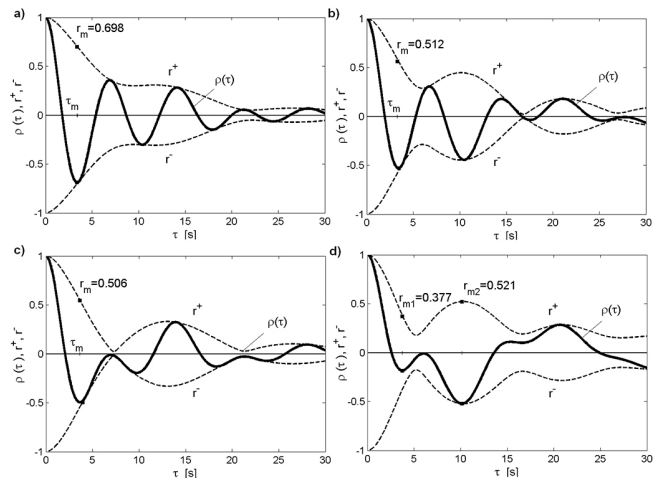**Table 2.** Characteristics of the individual spectral components.

| $H_s$ (m) | $T_p$ (s) | $L_p$ (m) | $d/L_p$ | $k_p d$ | $\varepsilon = k_p \sigma$ | $\Delta$ | BFI |
|---|---|---|---|---|---|---|---|
| 3.6 | 7 | 76.5 | 1.31 | 8.213 | 0.074 | 0.09 | 1.04 |
| 3.6 | 14 | 306.0 | 0.33 | 2.053 | 0.019 | 0.05 | 0.23 |
| 3.6 | 20 | 624.5 | 0.16 | 1.006 | 0.009 | 0.03 | 0.13 |
| 4.6 | 7 | 76.5 | 1.31 | 8.213 | 0.095 | 0.09 | 1.33 |
| 2.3 | 14 | 306.0 | 0.33 | 2.053 | 0.012 | 0.05 | 0.15 |
| 2.3 | 20 | 624.5 | 0.16 | 1.006 | 0.006 | 0.03 | 0.09 |

BFI and the increased probability of rogue waves in the time series. Consequently, the BFI estimate associated with the high-frequency counterpart of the bimodal spectra indicates possible development of an extreme event down the basin. Statistically this will be reflected in large departures of the tails of the wave height distributions from the Rayleigh law and the crest/trough distributions from the weakly nonlinear predictions.

Figure 2 illustrates wave spectra estimated at the first probe for the four cases of following mixed sea states. The row spectra have been block-averaged over $(\text{dof}/4) + 1$ adjacent values, with $\text{dof} = 400$. The first step in the analysis of the bimodal spectra is to apply criteria for identification and separation of the two components. A set of criteria proposed by Guedes Soares and Nolasco (1992) requires that the local maxima and minima be identified over eight frequency bands, such that the smaller peak is considered valid if its magnitude is equal to or 15 % greater than the larger peak. Furthermore, the trough between the two peaks must be less than the lower confidence bound of the smaller spectral peak. It should be mentioned here that this simple approach showed better accuracy when compared to a more comprehensive one (Ewans et al., 2006).

Having the two spectral counterparts separated, the relative contribution of the components is quantified by the ratio of the zero moments of the wind sea, $m_{0\,\text{ws}}$, and the swell, $m_{0\,\text{sw}}$ – the sea–swell energy ratio (SSER) (Rodríguez and Guedes Soares, 1999). The same SSER limits as for the bimodal crossing seas were imposed here to classify the mixed seas with the following wave trains (see Petrova and Guedes Soares, 2011): wind dominated sea (SSER > 1.6); sea-swell energy equivalent sea (0.9 < SSER < 1.6); swell-dominated sea (SSER > 1.6). Consequently, it results that: (1) 8228–8229 are wind sea dominated (Fig. 2a and b); (2) 8230 (Fig. 2c), as well as 8231 (Fig. 2d), can be described as sea-swell energy equivalent sea states, though comparing the profiles of the autocorrelation functions, $\rho(\tau)$, in Fig. 3, one can see that the profile in Fig. 3d (run 8231) resembles a swell-dominated case with a secondary smaller minimum before the global one.

Contrary to the crossing mixed seas, which showed pronounced variation of the spectral energies of wind sea and



**Figure 2.** Wave spectra at the first probe for mixed following seas: (a) 8228, (b) 8229, (c) 8230 and (d) 8231.



**Figure 3.** Autocorrelation functions associated with the wave spectra in Fig. 2: (a) 8228, (b) 8229, (c) 8230 and (d) 8231.

swell with the distance (Table 1 in Petrova and Guedes Soares, 2009), the energies of the spectral counterparts in the present study keep relatively unchanged during the wave propagation along the tank (Fig. 4). An exception is run 8231 with identical significant wave heights for the two JONSWAP components and larger intermodal distance (Fig. 4d). A reduction in the energy of the high-frequency counterpart occurs along the tank which can be due to breaking. However, following Babanin et al. (2007), wave breaking can be expected only if the mean steepness $\varepsilon$ exceeds 0.1. The initial conditions in the present study demonstrate $\varepsilon < 0.1$.

The deep water conditions for the individual spectral components are validated by the additional information in Table 2 showing the relative water depth in terms of $d/L_p$ and $k_p d$. This information is relevant to the wave stability, as far as $k_p d < 1.36$ describes water depth conditions
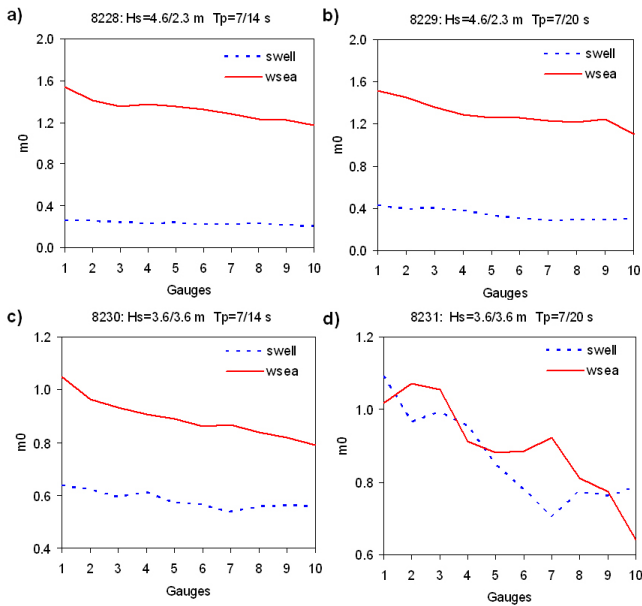
**Figure 4.** Following seas: variation with the distance of the spectral energies of the wind sea and swell components.



**Figure 5.** Evolution along the tank of the high-frequency spectral counterparts of the mixed following seas: **(a)** 8228, **(b)** 8229, **(c)** 8230 and **(d)** 8231.

where the wave train is stable to side-band perturbations (Mori and Yasuda, 2002). The values in Table 2 show that the short-period wave system ($T_p = 7$ s) fulfils the deep water inequality: $d/L_{pws} > 1/2$, where $L_{pws} = 76.5$ m. The long-period waves with $T_p = 14$ s do not fulfil the deep water condition, since $d/L_p < 1/2$, though still fulfilling $k_p d > 1.36$. The sea state with $T_p = 20$ s describes both intermediate water depth waves and stable wave modes according to the above inequality.

The development of modulational instability is accompanied by some typical changes in the spectral shape: broadening of the spectrum, downshift of the peak frequency, reduction of the tail (Janssen, 2003; Onorato et al., 2006b; Toffoli et al., 2008). The distance from the wavemaker is measured in multiples of the wave length corresponding to the high-frequency spectral peak, $L_p = 76.5$ m ($T_p = 7$ s). Figure 5 shows in logarithmic scale the changes in the shape of the high-frequency spectral component at three locations along the tank: $6.5L_p$ (gauge 1), $20L_p$ (gauge 5) and $33L_p$ (gauge 9). The abscissa illustrates the frequencies scaled by the spectral mode at gauge 1. The ordinate shows the magnitude of the spectral energy scaled by the spectral peak magnitude at gauge 1. It can be observed that as the waves advance along the tank the spectral tail reduces, the spectral peak diminishes and shifts downwards. Such results have been reported by e.g. Trulsen and Dysthe (1997) for numerical simulations, as well as by Onorato et al. (2006b), Fedele et al. (2010), for laboratory experiments. A slightly different pattern of change is seen for experiment 8231 (Fig. 5d): the increase of the spectral peak magnitude at the second and third probes results in normalized peak magnitudes larger than 1. This situ-
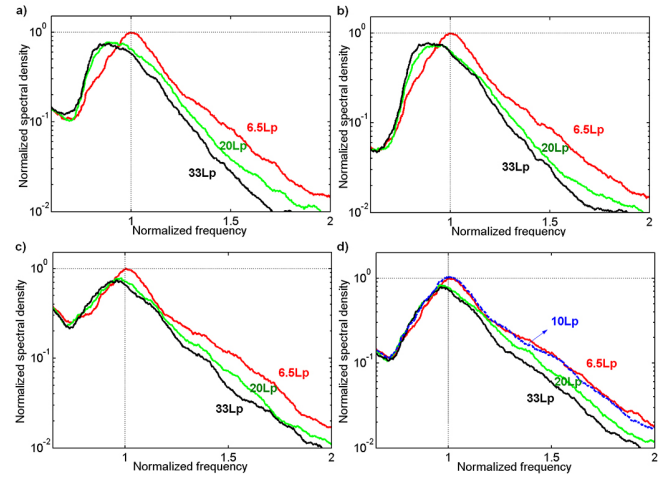
ation is demonstrated by the blue dotted line in the plot, corresponding to the spectral density curve at the second gauge ($\sim 10L_p$). The spectral changes described above can be also observed for the crossing bimodal seas, as can be seen in Fig. 6a–c for $\theta = 60$, 120 and 90°, respectively. The low-frequency spectral counterparts are not illustrated in Figs. 5 and 6, since they do not suffer the changes described above. Only small reduction of the spectral peak magnitudes occurs for the following systems with larger frequency shift, but the peaks remain at the same frequency. Consequently, one can assume that if the increased wave nonlinearity along the basin can be attributed to modulational instability, the latter should take place over the high-frequency range of the spectrum, especially when it is characterized by large BFI.

Figure 7a and b illustrate the spectral broadening over the high-frequency range in terms of $\Delta_{ws}$ for the following and crossing mixed seas, respectively. The maxima for the two following seas with combination $T_p = 7/14$ s (8228 and 8230) are reached at gauge 7. In particular, the observed increase for run 8230 is estimated at 42 % (Fig. 7a). The broadest high-frequency spectrum for 8229 is estimated later, at gauge 8. Run 8231, on the other hand, is characterized by the same initial characteristics of the bimodal spectrum as the crossing seas ($H_s = 3.6/3.6$ m, $T_p = 7/20$ s) and shows a maximum of $\Delta_{ws}$ at the same gauge as the crossing seas: gauge 6 (Fig. 7a and b).
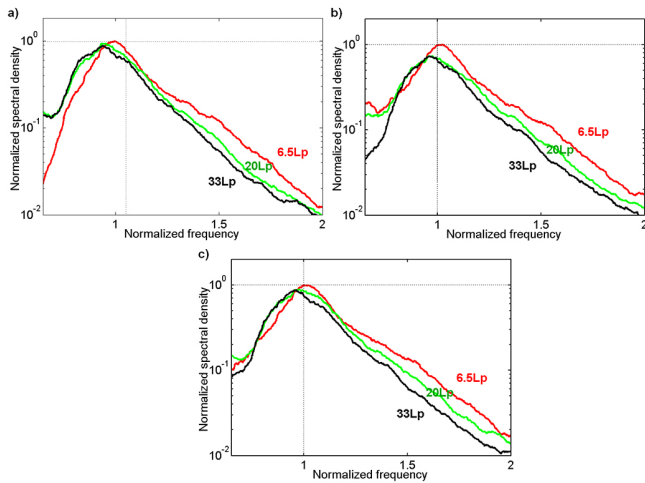
**Figure 6.** Evolution along the tank of the high-frequency spectral counterparts of the mixed crossing seas: **(a)** $\theta = 60°$, **(b)** $\theta = 120°$ and **(c)** $\theta = 90°$.



**Figure 7.** Changes in the width of the wind sea spectral component with the distance for: **(a)** following; **(b)** crossing mixed seas.

## 3 Experimental results: nonlinear wave statistics

The self-focusing effects observed for narrow spectra with large initial steepness can affect significantly the wave statistics. Thus, attention is given here first to some statistical quantities indicating nonlinearity and, in particular, to those indicating the possible presence of large-amplitude waves in the wave records.

Within the weakly nonlinear assumption, the non-Gaussian sea surface is considered a linear superposition of free modes modified by second-order bound harmonics. The resultant wave profiles display higher sharper crests and shallower rounded troughs. The vertical wave asymmetry is quantified by the normalized third-order cumulant $\lambda_{30}$ – the coefficient of skewness, calculated from the surface elevation, $\eta$, and its Hilbert transform, $\hat{\eta}$, as

$$\lambda_{mn} = \frac{\langle \eta^m \hat{\eta}^n \rangle}{\sigma^{m+n}}, \quad m + n = 3. \quad (2)$$

The positive skewness coefficient illustrates greater probability of occurrence of large positive displacements of the water surface than of large negative displacements. On the other hand, the increased frequency of encountering large crest-to-trough excursions due to third-order nonlinear wave–wave interactions is quantified by the fourth-order normalized cumulant, $\lambda_{40}$ – the coefficient of kurtosis, or by the sum of fourth-order joined cumulants $\Lambda = \lambda_{40} + 2\lambda_{22} + \lambda_{04}$. These two fourth-order statistics are used as higher-order corrections in the distribution models for wave crests, troughs and heights. The fourth-order normalized joint cumulants are presented in the following generalized form (Tayfun and Lo, 1990):

$$\lambda_{mn} = \frac{\langle \eta^m \hat{\eta}^n \rangle}{\sigma^{m+n}} + (-1)^{m/2}(m-1)(n-1), \quad m+n = 4. \quad (3)$$
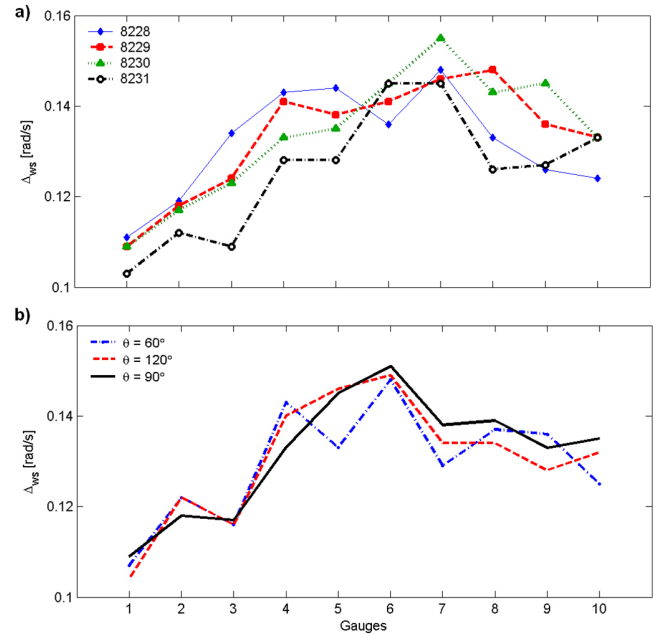
The nonlinear contributions to the coefficient of kurtosis are due to: (1) bound waves, where the associated correction is of order $O(\varepsilon^2)$, with $\varepsilon$ being the sea state steepness, so that for weakly nonlinear waves this effect is negligible, and (2) near-resonant interactions (Benjamin–Feir type instability), such as for relatively narrow spectra and long-crested waves the latter factor is dominant and gives rise to large deviations from Gaussianity (Janssen, 2003; Onorato et al., 2005; Mori and Janssen, 2006). The dependence of the spectral broadening and the kurtosis on BFI was theoretically shown by Janssen (2003), Mori and Janssen (2006), or observed experimentally by Onorato et al. (2004); Onorato et al. (2006b); Toffoli et al. (2008). However, the coefficient of kurtosis is proportional to the squared BFI only for long-crested seas (Gramstad and Trulsen, 2007).

Tables 3–6 summarize the overall averages of the third- and fourth-order cumulants estimated from the 15 min (full-scale) segmental series, each containing approximately 120 waves. The segmental analysis aims at avoiding possible non-stationarity in the original time series. The third-order corrections due to free waves are reflected by the key parameter $\Lambda$. One can see that the waves close to the wave generator have nearly Gaussian statistics ($\Lambda$ is usually the smallest there, and in two of the cases is practically zero), which can be expected since each of the unidirectional wave trains is a linear superposition of harmonics within the random amplitude/phase wave model. However, $\Lambda$ increases appreciably away from the wavemaker, which can be explained with the development of modulational instability.

**Table 3.** Overall statistical averages from 15 min segments for 8228: $H_s = 4.6/2.3$ m, $T_p = 7/14$ s.

| Gauge | $\sigma$ | $\lambda_{30}$ | $\lambda_{40}$ | $\lambda_{04}$ | $\lambda_{22}$ | $\Lambda$ |
|---|---|---|---|---|---|---|
| 1 | 1.339 | 0.267 | 0.165 | 0.009 | 0.029 | 0.233 |
| 2 | 1.291 | 0.225 | 0.296 | 0.156 | 0.076 | 0.603 |
| 3 | 1.257 | 0.225 | 0.355 | 0.153 | 0.085 | 0.678 |
| 4 | 1.265 | 0.228 | 0.410 | 0.178 | 0.098 | 0.785 |
| 5 | 1.256 | 0.219 | 0.308 | 0.171 | 0.080 | 0.638 |
| 6 | 1.240 | 0.222 | 0.353 | 0.183 | 0.090 | 0.717 |
| 7 | 1.225 | 0.218 | 0.321 | 0.172 | 0.083 | 0.659 |
| 8 | 1.206 | 0.206 | 0.465 | 0.372 | 0.140 | 1.116 |
| 9 | 1.194 | 0.200 | 0.380 | 0.310 | 0.115 | 0.920 |
| 10 | 1.170 | 0.212 | 0.498 | 0.364 | 0.144 | 1.150 |

**Table 4.** Overall statistical averages from 15 min segments for 8229: $H_s = 4.6/2.3$ m, $T_p = 7/20$ s.

| Gauge | $\sigma$ | $\lambda_{30}$ | $\lambda_{40}$ | $\lambda_{04}$ | $\lambda_{22}$ | $\Lambda$ |
|---|---|---|---|---|---|---|
| 1 | 1.396 | 0.240 | 0.107 | −0.023 | 0.014 | 0.112 |
| 2 | 1.354 | 0.200 | 0.079 | 0.021 | 0.017 | 0.135 |
| 3 | 1.323 | 0.229 | 0.236 | 0.067 | 0.051 | 0.404 |
| 4 | 1.289 | 0.199 | 0.325 | 0.146 | 0.079 | 0.629 |
| 5 | 1.253 | 0.187 | 0.324 | 0.247 | 0.095 | 0.761 |
| 6 | 1.243 | 0.199 | 0.366 | 0.241 | 0.102 | 0.810 |
| 7 | 1.226 | 0.238 | 0.340 | 0.190 | 0.089 | 0.707 |
| 8 | 1.223 | 0.164 | 0.431 | 0.355 | 0.131 | 1.048 |
| 9 | 1.238 | 0.135 | 0.288 | 0.246 | 0.089 | 0.712 |
| 10 | 1.183 | 0.171 | 0.359 | 0.245 | 0.101 | 0.807 |

**Table 5.** Overall statistical averages from 15 min segments for 8230: $H_s = 3.6/3.6$ m, $T_p = 7/14$ s.

| Gauge | $\sigma$ | $\lambda_{30}$ | $\lambda_{40}$ | $\lambda_{04}$ | $\lambda_{22}$ | $\Lambda$ |
|---|---|---|---|---|---|---|
| 1 | 1.299 | 0.155 | 0.054 | −0.001 | 0.009 | 0.071 |
| 2 | 1.260 | 0.155 | 0.142 | 0.075 | 0.037 | 0.292 |
| 3 | 1.237 | 0.143 | 0.182 | 0.166 | 0.058 | 0.465 |
| 4 | 1.231 | 0.167 | 0.218 | 0.124 | 0.057 | 0.456 |
| 5 | 1.207 | 0.109 | 0.249 | 0.184 | 0.072 | 0.577 |
| 6 | 1.192 | 0.220 | 0.357 | 0.205 | 0.094 | 0.751 |
| 7 | 1.184 | 0.158 | 0.136 | 0.109 | 0.041 | 0.327 |
| 8 | 1.181 | 0.177 | 0.282 | 0.160 | 0.074 | 0.591 |
| 9 | 1.170 | 0.140 | 0.360 | 0.229 | 0.099 | 0.788 |
| 10 | 1.158 | 0.156 | 0.305 | 0.198 | 0.084 | 0.671 |

**Table 6.** Overall statistical averages from 15 min segments for 8231: $H_s = 3.6/3.6$ m, $T_p = 7/20$ s.

| Gauge | $\sigma$ | $\lambda_{30}$ | $\lambda_{40}$ | $\lambda_{04}$ | $\lambda_{22}$ | $\Lambda$ |
|---|---|---|---|---|---|---|
| 1 | 1.448 | 0.123 | −0.022 | −0.063 | −0.014 | −0.112 |
| 2 | 1.423 | 0.139 | 0.029 | −0.083 | −0.009 | −0.071 |
| 3 | 1.428 | 0.138 | 0.000 | −0.037 | −0.006 | −0.048 |
| 4 | 1.364 | 0.181 | 0.100 | 0.043 | 0.024 | 0.191 |
| 5 | 1.313 | 0.126 | 0.118 | 0.126 | 0.041 | 0.327 |
| 6 | 1.285 | 0.096 | 0.172 | 0.094 | 0.045 | 0.355 |
| 7 | 1.273 | 0.150 | 0.199 | 0.163 | 0.060 | 0.482 |
| 8 | 1.258 | 0.124 | 0.188 | 0.237 | 0.071 | 0.567 |
| 9 | 1.238 | 0.123 | 0.101 | 0.158 | 0.044 | 0.347 |
| 10 | 1.193 | 0.069 | 0.113 | 0.208 | 0.054 | 0.429 |

The coefficient of skewness fulfils the identity $\lambda_{30} = 3\lambda_{12}$, thus being in agreement with the second-order wave theory (Tayfun and Lo, 1990; Tayfun, 1994). The remaining joint third-order cumulants, $\lambda_{03}$ and $\lambda_{21}$, as well as the joint fourth-order cumulants $\lambda_{31}$ and $\lambda_{13}$ are nearly zero. However, the fourth-order cumulants $\lambda_{40}$, $\lambda_{22}$, $\lambda_{04}$ and thus the cumulant sum $\Lambda$ assume rather large values with respect to $\lambda_{30}$, exceeding $O(\lambda_{30}^2)$ for weakly nonlinear waves. The largest values of $\Lambda$ are observed over the last three gauges in the tank. In particular, the maxima of the wind-sea dominated mixed seas show $\Lambda \geq 1$ (tables 3 and 4), while those of the sea-swell energy equivalent following mixed seas are smaller (tables 5 and 6). The nonlinear pattern reflected by the wave statistics in mixed seas with following wave trains corroborates recent conclusions for mechanically generated single unidirectional irregular waves influenced by higher-order effects (Cherneva et al., 2009), as well as for mixed crossing wave systems (Petrova et al., 2013).

The wave statistics for test 8231 (Table 6) can be directly compared with the statistics from bimodal crossing seas analysed previously by Petrova et al. (2013), since the generated sea states have identical individual spectral characteristics ($H_s = 3.6/3.6$ m and $T_p = 7/20$ s). The comparison

shows that the nonlinear statistics of the mixed following sea states are generally lower. In particular, the maximum value of $\Lambda$ for the following sea is $\Lambda_{max} = 0.567$ (gauge 8), compared to $\Lambda_{max} = 1.571$ (gauge 10) for $\theta = 90°$ and $\Lambda_{max} = 1.347$ (gauge 9) for $\theta = 120°$. For the smallest angle of crossing, $\theta = 60°$, a local maximum is reported at gauge 8: $\Lambda_{max} = 0.673$.

Consequently, the amplitudes and heights of the largest waves associated with the relatively large values of $\Lambda$, such as those usually registered at the last probes, can be suitable for comparisons with theoretical probabilistic models corrected for third-order nonlinearity.

## 4 Theoretical distributions of wave amplitudes and crest-to-trough heights

The zero-mean sea surface displacement $\eta$ at a fixed point, in time $t$, is written as $\eta = \xi(t)\cos\varphi(t)$, where $\xi \geq 0$ and $\varphi$ stand for the random amplitude and phase functions slowly varying in time. Though being valid for both linear and nonlinear waves in the most general case, the linear waves have independent $\xi$ and $\varphi$, such that $\xi$ is Rayleigh distributed and $\varphi$ is uniformly random over an interval of $2\pi$ (Rice, 1945). Furthermore, in the narrowband case the amplitude $\xi$ nearly

coincides with the global maxima (wave crests) and global minima (wave troughs) of $\eta$. As a result, the crest and trough amplitudes of linear waves can be approximated with the Rayleigh law. Letting $\nu$ be the spectral bandwidth (Longuet-Higgins, 1975), this approximation will introduce errors of order $O(\nu^2/\xi)$, which reduce when $\nu^2 \ll 1$ and/or $\xi \gg 1$ (Tayfun and Lo, 1990).

The Rayleigh exceedance probability of $\xi$ normalized by the root-mean-square surface displacement, $\sigma$, has the form

$$E(\xi) = \exp(-\xi^2/2), \quad \xi \geq 0. \tag{4}$$

Further assuming a narrowband spectrum, $\nu^2 \ll 1$, allows approximation of the normalized linear crest-to-trough wave height as twice the wave envelope, $H \approx 2\xi$, and by a change of variables in Eq. (4) one comes to (Longuet-Higgins, 1952)

$$E_{H \approx 2\xi}(h) = \exp(-h^2/8), \quad h \geq 0. \tag{5}$$

The second-order nonlinearity of the free surface is a result of the linear superposition of free waves modified by second-order bound harmonics. Various models describing the distributions of wave amplitudes, phases, crests and troughs in weakly nonlinear waves have been elaborated so far (Tayfun and Lo, 1990; Tayfun, 1994; Tayfun 2006, 2008). For instance, the second-order wave crest $\xi^+$ and trough $\xi^-$ are expressed as (Tayfun, 2006)

$$\xi^{\pm} = \xi \pm \frac{1}{2}\mu\xi^2, \tag{6}$$

where $\mu$ is a dimensionless steepness parameter. For narrowband waves, $\mu = \lambda_{30}/3$, while in the more general case, $\mu$ can assume slightly different forms, as shown by Tayfun (2006). Following Tayfun (2008), the exceedance probabilities of $\xi^+$ and $\xi^-$ are expressed as

$$E_{\xi^+}(z) = \exp\left[-\frac{(\sqrt{1+2\mu z}-1)^2}{2\mu^2}\right] \tag{7}$$

$$E_{\xi^-}(z) = \exp\left\{-\frac{1}{2}\left[z\left(1+\frac{1}{2}\mu z\right)\right]^2\right\} \tag{8}$$

where $\mu = \lambda_{30}/3$.

Third-order corrections due to second- and third-order bound waves in a weakly nonlinear wave field are typically of order $O(\lambda_{30}^2)$. Consequently, their contribution is rather small, since $\lambda_{30} \ll 1$ for deep water storm waves. However, mechanically generated extremely large waves display amplitudes and heights that can deviate significantly from the linear and second-order predictions, which can be explained by third-order quasi-resonant interactions among free modes. These tend to amplify the wave statistics and increase the occurrence frequency of large events, leading to long tails in the observed empirical distributions (Mori et al., 2007; Cherneva et al., 2009; Fedele et al., 2010).

Modifying Eqs. (7) and (8) to include the third-order effects in terms of the parameter $\Lambda$ results in the approximate forms (Tayfun and Fedele, 2007; Tayfun, 2008)

$$E_{\xi^+}(z) = \exp\left[-\frac{(\sqrt{1+2\mu z}-1)^2}{2\mu^2}\right]\left[1+\frac{\Lambda}{64}z^2\left(z^2-4\right)\right] \tag{9}$$

$$E_{\xi^-}(z) = \exp\left\{-\frac{1}{2}\left[z\left(1+\frac{1}{2}\mu z\right)\right]^2\right\}\left[1+\frac{\Lambda}{64}z^2\left(z^2-4\right)\right] \tag{10}$$

For brevity, Eqs. (7) and (8) and Eqs. (9) and (10) are referred to in the text and in the plots as NB and NB-GC models, respectively. The abbreviation GC stands for the correction term due to the Gram–Charlier approximation for the marginal distribution of wave envelopes.

The large crest-to-trough wave heights are unaffected by second-order nonlinearities (Tayfun, 2011). Regardless of the spectral width, the large wave heights in simple wind seas are well predicted by the asymptotic models of Tayfun (1990) and Boccotti (1989). The model of Boccotti is approximately exact for heights exceeding $3.5\sigma$, applies to spectra of any bandwidth and depends on two parameters, while the model of Tayfun is correct to $O(\nu)$, but requires a single parameter. These two models, in particular Boccotti's distribution, were validated using oceanic measurements and simulations (Boccotti, 2000; Tayfun and Fedele, 2007; Casas-Prat and Holthuijsen, 2010). The lower bound approximation of Tayfun's model was also found to describe well the data from swell-dominated bimodal crossing sea states (Petrova et al., 2013). This model was preferred, since it has a somewhat larger range of validity than Boccotti's model, and the single parameter allows generalization to swell-dominated mixed sea states or sea states with comparable sea-swell energies where the autocorrelation function does not have monotonically decaying shape and the global minimum is no longer the first one (Fig. 3d).

The lower bound approximation of the model of Tayfun (1990) has the form

$$E(h) \approx \left(\frac{1+r_m}{2r_m}\right)^{1/2}\exp\left\{-\frac{h^2}{4(1+r_m)}\right\} \tag{11}$$

for $h > \sqrt{2\pi}$; $r_m$ is a dimensionless parameter defined as $r_m = r(T_m/2)$, as illustrated in Fig. 3a–c, where $r =$ envelope of the normalized autocorrelation function, and $T_m = 2\pi m_0/m_1$ with $m_i = i$th ordinary spectral moment. To account for the secondary minimum before the global one in the profile of the autocorrelation function, the parameter $r_m$ is reformulated as a function of the normalized wave height $h$ in the form (Petrova et al., 2013)

$$r_m(h) = (r_{m1}+r_{m2}) - r_{m1}\left[1 - \exp\left(-\frac{h}{\sqrt{1+\alpha^2}}\right)\right] \tag{12}$$

where $\alpha = T_{psw}/T_{pws}$ is a dimensionless ratio of the peak period $T_{psw}$ of the low-frequency spectrum to the peak period $T_{pws}$ of the high-frequency spectrum; $r_{m1}$ and $r_{m2}$ designate

the values of the envelope $r(\tau)$ at the secondary minimum of ACF and at the global minimum of ACF, respectively (see Fig. 3d). Equation 12 then yields $r_m(h) \approx r_{m2}$ for $h \gg 1$, so as the distribution of the largest waves will be based on the global minimum of the autocorrelation function.

The asymptotic distributions are restricted to linear and second-order waves only. Higher-order corrections, such as those due to third-order nonlinear interactions in relatively narrowband long-crested waves, either generated mechanically in laboratory experiments or simulated numerically, can be accounted for by Gram–Charlier (GC) series expansions. Longuet-Higgins (1963) used for the first time series approximations to represent the nonlinearity of the sea surface displacement and its related features. Bitner (1980) demonstrated their applicability to the representation of shallow water waves and extended their use to different wave parameters, among which are wave envelopes, heights and phases. Later, the series approach was more systematically applied by Tayfun and Lo (1990) and Tayfun (1994), focusing on the distributions of wave envelopes and phases of a weakly nonlinear deep water wave field. Further elaborations and applications for second- and third-order waves can be found in Mori and Janssen (2006), Tayfun and Fedele (2007), and Tayfun (2008).

In particular, the Gram–Charlier wave height model used here to fit the laboratory observations is taken in the form proposed by Tayfun and Fedele (2007):

$$E_{H=2\xi}(h) = \exp\left(-\frac{h^2}{8}\right)\left[1 + \frac{\Lambda}{1024}h^2\left(h^2 - 16\right)\right]. \quad (13)$$

At this point, it must be noted that all distributions introduced above refer to one-peak spectra, which generally describe severe sea conditions (wind–sea dominated spectrum). Moderate and low sea states, on the other hand, often have a contribution by at least two wave systems (Guedes Soares, 1984; Guedes Soares and Nolasco, 1992; Lucas et al., 2011). Though the available theoretical models do not assume a second wave train, it seems that they have a broader application in their predictions, since the results show that in particular cases they can either represent well the data or provide a qualitative description of the observed tendencies.

## 5 Experimental results: probability distributions

### 5.1 Probability distributions of wave crests and troughs

The experimental data consist of pooled samples of crests/troughs from the 15 min segmental analysis. The wave crests, $\xi^+$, are determined as the global positive maxima of the zero-crossing waves and are scaled by the local segmental standard deviation of the 15 min segments, $\sigma$. The wave troughs, $\xi^-$, are defined as the global negative minima of the zero-crossing waves and are also scaled by the segmental $\sigma$. The crest and trough exceedance probabilities, $E_{\xi^+}$ and $E_{\xi^-}$,

respectively, are approximated by: (1) the second-order narrowband models, designated by NB in the plots (Eqs. 7 and 8); (2) the modified narrowband models including third-order corrections, designated by NB-GC (Eqs. 9 and 10), and (3) the Rayleigh form, designated by $R$ (Eq. 4).

The second-order individual waves are expected to exhibit high steep crests and shallow flat troughs, which results in a positive skewness coefficient. However, as one can see next, the experimental crests largely exceed the second-order predictions. Moreover, the troughs tend to be deeper than predicted by the second-order theory. These discrepancies can only be explained by higher-order nonlinear wave–wave interactions, since the corrections due to bound modes just slightly increase the non-Gaussian statistics.

The first column of Fig. 8 illustrates the distributions of wave amplitudes for test 8228 ($H_s = 4.6/2.3$ m, $T_p = 7/14$ s) at three locations along the basin: at gauge 1 where $\Lambda$ is a minimum (Fig. 8a); at gauge 8 where $\Lambda$ shows a local maximum (Fig. 8b), and at the last gauge: gauge 10 (Fig. 8c). The measured crest heights are shown as full triangles and the trough depths as full circles. The total number of waves in each pooled sample is designated as $N$ in the plots. It can be seen that for the smallest $\Lambda$ (Fig. 8a) the wave crests in the midrange are largely underestimated by all models. With the distance, the wave crests show gradual improvement in the agreement with NB-GC, which is obvious in Fig. 8b and c. Large wave crests exceeding $5\sigma$ are registered by probes 4 and 8, and as one can see in Fig. 8b, such a crest extreme is only slightly underestimated by NB-GC. The wave troughs, on the other hand, are fitted well by NB-GC up to approximately $3\sigma$ for all gauges. At gauge 1 (Fig. 8a), however, it can be assumed that NB $\approx$ NB-GC. The empirical tail constructed of the deepest eight troughs exhibits large variation and usually corresponds to probabilities of exceedance lower than those predicted by NB-GC.

The plots in the second column of Fig. 8 illustrate the distributions for test 8229 ($H_s = 4.6/2.3$ m, $T_p = 7/20$ s). The generated spectral conditions differ from those in experiment 8228 by imposing a larger intermodal distance while the sea-swell energy ratio is kept unchanged. The associated statistics are less nonlinear (Table 4). It can be observed that both empirical and theoretical distributions become narrower. However, the pattern of change along the tank is similar to 8228. The wave crests at the first three gauges are largely underestimated by the theoretical models over the midrange ($2$–$4\sigma$) (Fig. 8d). This discrepancy reduces with the distance, so that the wave crests measured by the second half of the gauges are in close agreement with NB-GC for $\xi^+ \leq 4$–$4.5\sigma$ (Figs. 8e and f). Similarly to test 8228, the largest crests, such as $\xi^+ > 5.5\sigma$, are registered again by probes 4 and 8. However, they appear as outliers in the sample, as seen in Fig. 8e. At the first three gauges, the troughs follow NB $\approx$ NB-GC and afterwards NB-GC up to approximately $3\sigma$.
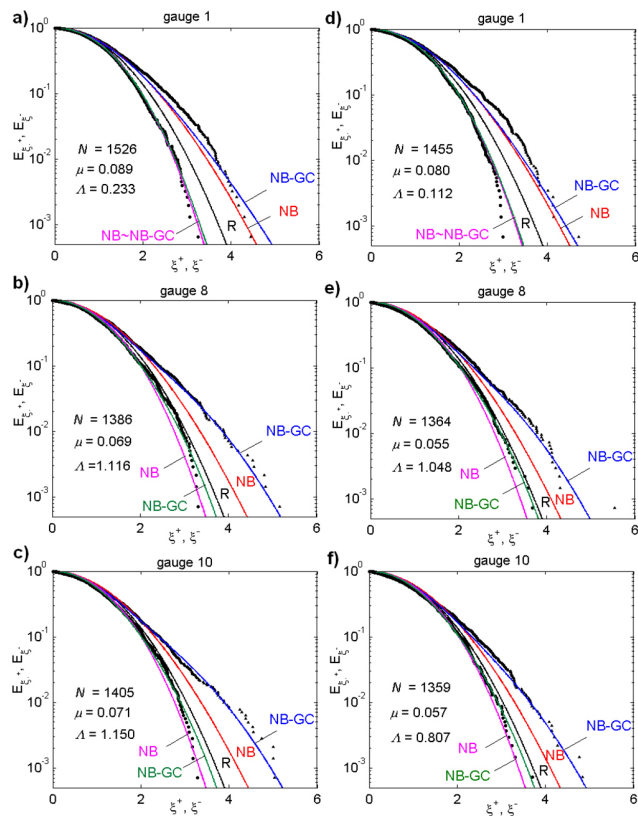
**Figure 8.** Exceedance distributions of wave crests and troughs along the tank for **(a–c)** test 8228 and **(d–f)** test 8229.



**Figure 9.** Exceedance distributions of wave crests and troughs along the tank for **(a–c)** test 8230 and **(d–f)** test 8231.

The results for the crest/trough distributions for run 8230 ($H_s = 3.6/3.6$ m, $T_p = 7/14$ s) are shown in Fig. 9a–c. The initial sea state conditions are less steep, as compared to 8228 and 8229, so that smaller third- and fourth-order statistics are observed (Table 5). In particular, $\lambda_{40} \approx \lambda_{30}^2$ at the first probe (Fig. 9a) which holds within the weakly nonlinear assumption for the wave process. Consequently, both the crest and trough amplitudes appear to be in good agreement with the second-order models (NB $\approx$ NB-GC). However, the coefficient of kurtosis suffers a significant change with the distance from the wavemaker. While at gauge 1 it is almost zero ($\lambda_{40} = 0.054$), at gauge 6 it is already comparable with the estimates for the more energetic runs: 8228 and 8229 (tables 3–6). This tendency is in agreement with the increasing discrepancies between the observations and the predicted exceedance probabilities of the linear model, especially for the data collected by the second half of the gauges. Figure 9b shows results for the maximum estimated $\lambda_{40}$, and one can see that the Gram–Charlier form fits perfectly the whole range of wave troughs, though it fails to predict the crests exceeding $4\sigma$. In Fig. 9c the trough tail is rather better fitted by $R$, though the deepest trough remains underpredicted. In both of the cases, the largest sampled crest is associated with a possible abnormal wave candidate, following the defi-
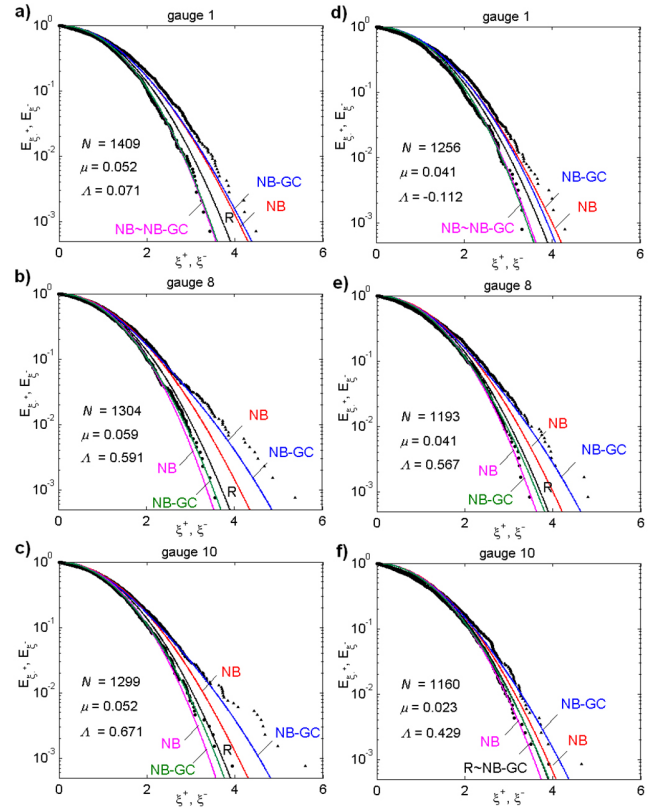
nition of Tomita and Kawamura (2000): $C_{\max}/H_s > 1.3$ and $H_{\max}/H_s > 2$.

The narrowest distributions belong to run 8231 ($H_s = 3.6/3.6$ m, $T_p = 7/20$ s), which differs from 8230 by the larger intermodal distance (compare Fig. 9a–c with Fig. 9d–f). As can be expected, the estimated non-Gaussian statistics for this case study are the smallest (see Table 6). The distributions show initial widening over the first half of the set of gauges and then again become narrow towards the last gauge. One can assume that the wave troughs generally follow the second-order model with some exceptions at the extreme tail for the first three gauges: troughs deeper than $3\sigma$ are overestimated by all models. The crests, on the other hand, tend to be underpredicted by all considered models for $\xi^+ > 3.5\sigma$. However, over the last three gauges, NB-GC is a reasonably good approximation of the crest data, except for the largest observations (Fig. 9e–f).

The results for test 8231 are suitable for comparison with the results for crossing bimodal seas discussed in Petrova et al. (2013), since 8231 has the same characteristics of the individual spectral components. Though the distribution results for the crossing seas are not illustrated here, it suffices to summarize that for the same initial sea state conditions, the addition of a second wave component crossing at an an-

gle increases the chance for deviation from the linear models with the distance from the wave generator. For larger angles of spread, on the other hand, the distributions of wave crests and troughs are better fitted by the second-order narrowband models. These results actually confirm the fact that the large shift between the main directions of the component wave systems in a mixed sea suppresses the modulational instability. Consequently, one encounters smaller wave amplitudes and heights at the lowest probability levels of the distribution tails, as already reported for numerically simulated waves (Onorato et al., 2006a; Shukla et al., 2006; Onorato et al., 2010; Toffoli et al., 2011) for waves modelled from the second-order theory (Toffoli et al., 2006), or in laboratory experiments (Toffoli et al., 2011). The most favourable angles of crossing for the occurrence of large wave events are reported to be in the range between 10 and 40°.

## 5.2 Probability distributions of wave crest-to-trough heights

Next, the exceedance probabilities of the measured wave heights, $E_h$, are discussed. All empirical distributions are estimated from the 15 min consecutive segments using the Weibull plotting position formula (Goda, 2000). The height of a wave is defined as the elevation difference between the wave crest and the adjacent trough, following either the up-crossing or the down-crossing wave definition. Since these differ, except for Gaussian sea, resulting in larger up-crossing wave heights, the experimental distributions presented next are constructed by averaging the two definitions for the ranked wave heights to obtain more stable estimates. Afterwards, they are normalized by the segmental $\sigma$. The Rayleigh form is used as a reference for the narrowband linear waves. It must be noted that the model of Tayfun (1990) appears in the plots as T1 when calculated with the original parameter $r_m$, and as T1$_h$ when the parameter is recalculated as $r_m = r_m(h)$ using Eq. (12). The results are plotted in Figs. 10 and 11 for the three locations along the tank already considered for the wave crests and troughs (gauges 1, 8 and 10). The wave height data are illustrated in the plots as full squares.

The first column of Fig. 10 illustrates the evolution of the wave height distribution along the tank for test 8228. Some characteristic distribution parameters and statistics are also included in the plots. It is seen in Fig. 10a (gauge 1) that though the sample follows the Rayleigh model up to approximately $5.5\sigma$, the tail of the distribution is increasingly overestimated by it. However, along the tank the tail gradually shifts up towards larger probabilities of exceedance. This shift is statistically justified by the increasing value of $\Lambda$, which is provided as an additional information in the plots. One can see that even for the largest values of $\Lambda$ (Fig. 10b and c) the wave heights are quantitatively better described by $R$, though $R$ slightly underestimates the tail at the last gauge (Fig. 10c). Applying the abnormality index of Dean (1990), it can be concluded that none of the observed wave height
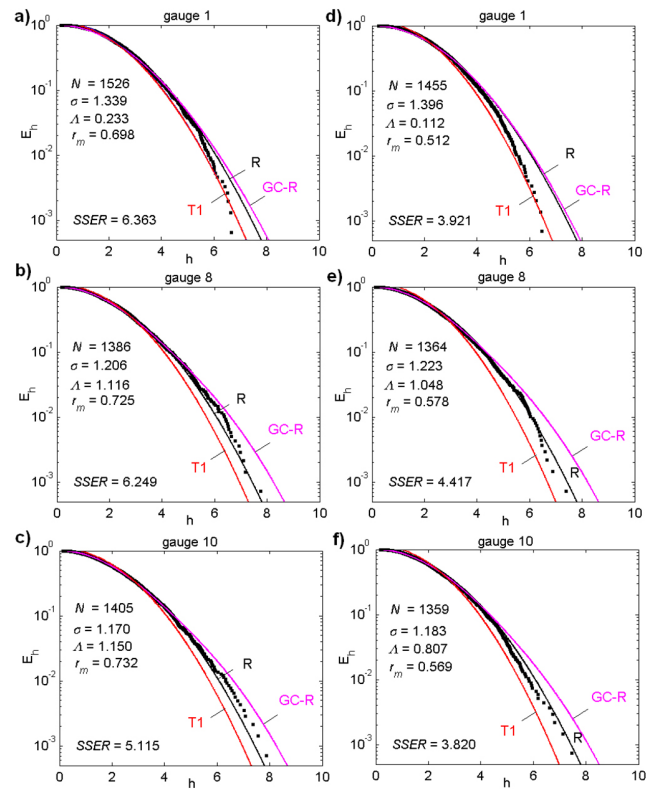


**Figure 10.** Exceedance distributions of wave heights along the tank for **(a–c)** test 8228 and **(d–f)** test 8229.

maxima for run 8228 can be classified as abnormal, since none of them exceeds $8\sigma$.

The second column of Fig. 10 shows the results for run 8229. At the first gauge (Fig. 10d) the distribution of Tayfun, T1, predicts most accurately the distribution tail ($h > 5\sigma$), since it reflects the increased spectral bandwidth due to the contribution of the low-frequency energy to the total spectrum. With the distance, the probability of encountering larger sampled waves increases, though the predictions of the Rayleigh distribution appear always as the upper limit for the probabilities of exceedance. The plots in Fig. 10e–f demonstrate that $R$ usually describes well the wave heights up to approximately $6\sigma$.

The initial conditions for test 8230 result in the most significant change in the empirical distribution along the tank: the empirical curve shifts from the best fit due to T1 (Fig. 11a) towards $R$ (Fig. 11b) and GC-R (Fig. 11c). However, GC-R slightly overpredicts the wave height extremes. Three of the probes during run 8230 recorded wave height maxima exceeding or close to the $8\sigma$ limit, as one can see in the examples in Fig. 11b and c. These waves can be classified as abnormal.

The results for test 8231 are illustrated in the second column of Fig. 11. The specific form of the associated autocorrelation functions, resembling the one in Fig. 3d, required
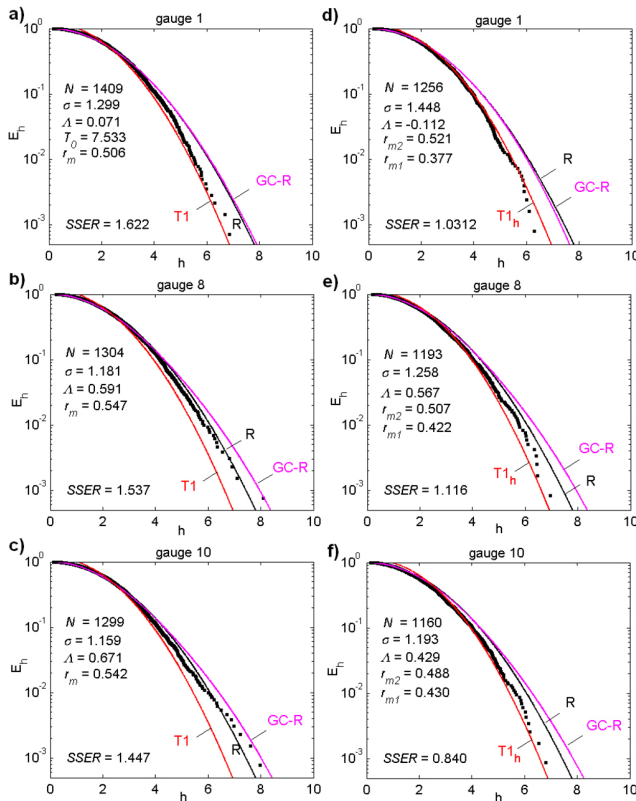
**Figure 11.** Exceedance distributions of wave heights along the tank for **(a–c)** test 8230 and **(d–f)** test 8231.

the use of Eq. (12) to recalculate the parameter $r_m$ in the model of Tayfun. The recalculated model is designated in the plots as T1$_h$. The recorded wave heights are smaller, as compared to those in run 8230, which corroborates the conclusion of Rodríguez et al. (2002) that the coexistence of two wave fields with different dominant frequencies but similar energy content reduces the exceedance probability of wave heights larger than the mean wave height. This effect becomes more pronounced when the intermodal distance increases. In the present study, the wave heights from the first half of the basin are well-fitted by T1$_h$ (Fig. 11d) and, though showing a tendency to increase towards gauge 8 (Fig. 11e), the largest measurements eventually reduce again and are favourably predicted by T1$_h$ (Fig. 11f).

The results for the distributions of wave crests, troughs and crest-to-trough wave heights for bimodal following seas presented above agree somewhat with the results for bimodal crossing seas in Petrova et al. (2013), showing again that the wave height statistics depends on the angle between the mean direction of the component wave systems and the propagated distance. For partially common directions of the crossing wave systems ($\theta = 60°$), the empirical exceedance probabilities of wave heights do not in general exceed $R$, which somewhat corroborates the findings of Cavaleri et al. (2012). For partially opposing directions ($\theta = 120°$), the nonlinear statis-

tics representative of large waves closer to the wavemaker, where the wave field energy is dominated by the swell, tend to T1$_h$. Away from the wavemaker, however, the third-order nonlinearities become significant, especially at the last four gauges. The distribution pattern at these gauges shows agreement with the GC-R over the range of the largest waves. On the other hand, run 8231, used for direct comparison with the crossing sea states, is characterized with the narrowest wave height distributions and, therefore, the data show the smallest deviations from the linear approximations. Furthermore, the empirical distributions are always overestimated by the Rayleigh law, as expected (Longuet-Higgins, 1983).

## 6 Removing the second- and third-order bound wave effects from the surface profile

The procedure of Fedele et al. (2010) has been applied to remove the second- and third-order bound wave contributions from the recorded surface elevation $\eta$. The non-skewed surface profile is obtained as

$$\tilde{\eta} = \eta - \frac{\beta}{2}\left(\eta^2 - \hat{\eta}^2\right) + \frac{\beta^2}{8}\left(\eta^3 - 3\eta\hat{\eta}^2\right) + O\left(\beta^3\right) \quad (14)$$

where $\hat{\eta}$ = Hilbert transform of $\eta$ and $\beta$ = parameter to be determined so that $\langle\tilde{\eta}^3\rangle = 0$.

Consequently, the procedure provides a way to assess the relevance of third-order nonlinearity due to free waves only. In particular, the vertical asymmetry in the wave profile is basically attributed to second-order bound harmonics and is expressed statistically by the positive skewness of the sea surface probability density function (see Tayfun 2008, for removing the second-order asymmetry only). Consequently, removing the vertical asymmetry due to both second- and third-order bound wave modes (the second and third terms in Eq. 14, respectively) leaves only the symmetric corrections to the free surface due to third-order free waves, which is statistically reflected by the positive coefficient of kurtosis.

In the following, Eq. (14) is applied to generate the non-skew surface profiles for run 8230 at the three locations which have been considered in Sect. 5 (gauges 1, 8 and 10). Test 8230 is the only experimental run where some of the largest registered wave events could be classified as abnormal with respect to the abnormality index. The empirical wave crest and trough distributions at gauge 1 are in agreement with the second-order models while the wave heights are largely overestimated by $R$ (Figs. 9a and 11a). At gauge 8, the NB-GC model predicts well the wave troughs over the entire data range but underestimates the wave crests exceeding $3\sigma$ (Fig. 9b). The wave height exceedance probabilities are limited by the Rayleigh model predictions, except for the largest event which is inconsistent with the rest of the sample (Fig. 11b). The wave field at gauge 10, on the other hand, is characterised with the largest fourth-order statistics, the maximum observed wave is classified as rogue in terms of

the abnormality index and the long distribution tail is built by a set of relatively large waves (Figs. 9c and 11c).

The plots in the first column of Fig. 12 illustrate segments of the nonlinear surface profiles around the largest crests for each of the three considered cases (thin black line), the second-order corrections extracted from them (dashed red line) and the resulting non-skew wave profiles (empty circles). The third-order bound wave corrections are not presented in the plots, since they appear to be of order $O(10^{-1})$ at the maximum crest, as compared to the second-order calculations, so they are hardly distinguishable from the mean water level. The plots in the second column of Fig. 12 illustrate the empirical distributions using the non-skewed series and their comparison with the relevant theoretical models. The wave heights are designated as full squares, the wave crests – as full triangles and the wave troughs – as full circles. It must be noted that the wave analysis regarding the non-skewed surface $\tilde{\eta}$ is also based on 15 min segments, so that the wave parameters are scaled by the segmental standard deviation, which is practically the same as the standard deviation of the original time series $\eta$. As a result of the applied procedure, the coefficient of skewness of $\tilde{\eta}$ becomes practically zero, as well as $\mu$; the fourth-order averages $\lambda_{40}$ and $\lambda_{22}$ reduce largely, while $\lambda_{04}$ remains nearly the same. As a result, the recalculated $\Lambda$ is also smaller.

The non-skew wave crests and troughs in Fig. 12d follow the Rayleigh curve fairly well. This implies symmetry of the wave profile around the mean water level. The wave height exceedance distribution remains almost unchanged, perfectly fitting $R$, which agrees with the conclusion that second-order effects have negligible influence on the large wave height statistics. The wave field associated with Fig. 12b and e (gauge 8) is characterized by moderately large initial value of $\Lambda$ (= 0.591) which is reduced to $\Lambda = 0.445$ for $\tilde{\eta}$. The distribution of wave troughs extracted from the non-skew series follows almost exactly $R$ over the observed interval. The wave crests, however, deviate significantly from the linear model implying that third-order corrections should be pertinent to this case. The wave height statistics by and large remain the same as before and are described qualitatively by $R$, though they keep slightly overestimated by it. The largest wave that appears as outlier among the sample of waves is less than $8\sigma$. The example in Fig. 12f illustrates the result for a record with a possible abnormal wave, characterized by relatively large $\Lambda$ (= 0.671), which diminishes to $\Lambda = 0.545$ in the non-skew series. Both wave crests and troughs are inconsistent with the Rayleigh distribution, demonstrating excess of probability. On the other hand, the largest observed wave heights are well represented by the Rayleigh distribution and the largest wave remains very close to the limit of $8\sigma$. Consequently, one can conclude that the modulational instability could be relevant to the last considered case.
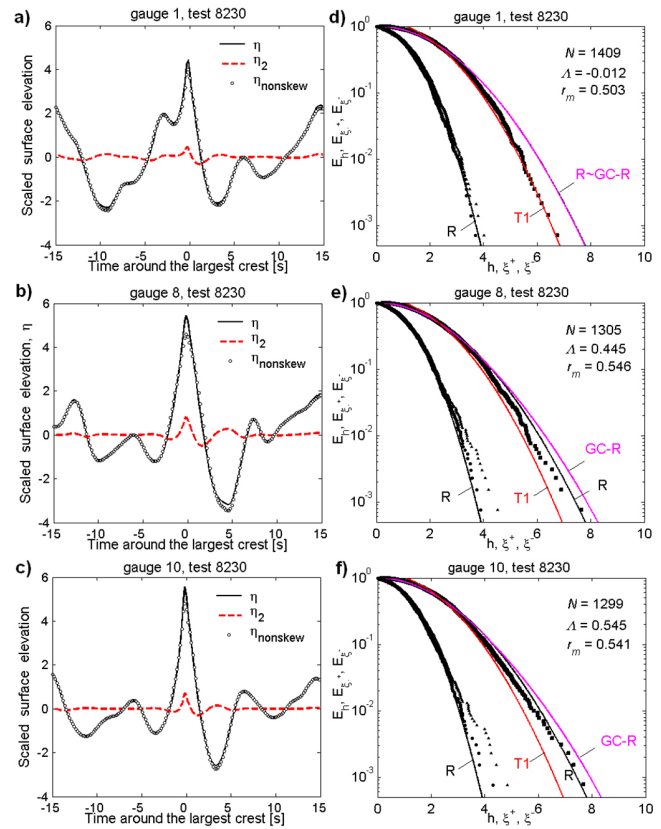


**Figure 12. (a–c)** Non-linear surface profile around the largest crest (thin line), second-order corrections (dashed line) and non-skew profile (circles); **(d–f)** distributions of crests, troughs and heights extracted from the non-skew surface series.

## 7 Conclusions

The paper presents an analysis of the probability distributions of crests, troughs and heights of deep water waves from mixed following sea states generated mechanically in the offshore basin at Marintek, and makes a brief comparison with previous results for mixed crossing seas from the same experiment. The random signals at the wavemaker in both types of considered mixed seas are characterized by bimodal spectra with individual JONSWAP components, following the model of Guedes Soares (1984).

In general, the wave nonlinearity is found to increase with the distance from the wavemaker. However, the nonlinear statistics of the following sea states are usually lower than for mixed crossing seas with identical initial spectral characteristics. This is obvious when comparing the mixed crossing seas with the results for test 8231. When the two wave systems propagate in the same direction, $\Lambda$ does not exceed 0.6, while for any of the mixed crossing seas this parameter attains much larger values, e.g. $\Lambda$ exceeds 0.9 for $\theta = 90°$; $\Lambda$ exceeds 1 for $\theta = 120°$.

The results for the distribution of wave heights for tests 8230 and 8231 corroborate the conclusion of Rodríguez et al. (2002) that the coexistence of two wave systems of different dominant frequencies but similar energy contents results in a reduction in the probability of wave heights larger than the mean, and this effect becomes more pronounced when the intermodal distance increases.

It is observed that the high-frequency spectral counterpart for both following and crossing seas shows a decrease in the peak magnitude and downshift of the peak with the distance, as well as a reduction of the spectral tail. These changes are typical for the evolution of spectra when modulational instability takes place. This result allows for association of the increasing probability of abnormal waves along the tank with possible Benjamin–Feir instability favoured by the steep narrowband conditions over the high-frequency range of the spectrum.

The results from removing the second- and third-order bound wave effects from the nonlinear surface profiles show that in some cases away from the wave generator the wave parameters of the non-skewed profiles continue deviating largely from the linear predictions, which proves the need for using higher-order models for the description of the wave data when free wave interactions become relevant.

Edited by: E. Bitner-Gregersen
Reviewed by: two anonymous referees

## References

Arena, F. and Guedes Soares, C.: Nonlinear crest, trough and wave height distributions in sea states with double-peaked spectra, J. Offshore Mech. Arct. Eng., 131, 041105, doi:10.1115/1.3160657, 2009.

Babanin, A., Chalikov, D., Young, I., and Savelyev, I.: Predicting the breaking onset of surface water waves, Geophys. Res. Lett., 34, L07605, doi:10.1029/2006GL029135, 2007.

Bitner, E.: Non-linear effects of the statistical model of shallow-water wind waves, Appl. Ocean Res., 2, 63–73, 1980.

Bitner-Gregersen, E. and Hagen, Ø.: Effects of two-peak spectra on wave crest statistics, in: Proceedings of the 22nd International Conference on Offshore Mechanics and Arctic Engineering, Cancun, Mexico, 8–13 June 2003, 1–8, 2003.

Boccotti, P.: On Mechanics of Irregular Gravity Waves, Atti Acc. Naz. Lincei, Memorie VIII, 1989.

Boccotti, P.: Wave Mechanics for Ocean Engineering, Elsevier Science, Amsterdam, 2000.

Boukhanovski, A. and Guedes Soares, C.: Modelling of multi-peaked directional wave spectra, Appl. Ocean Res., 31, 132–141, 2009.

Casas-Prat, M. and Holthuijsen, L. H.: Short-term statistics of waves observed in deep water, J. Geophys. Res., 115, 5742–5761, 2010.

Cavaleri, L., Bertotti, L., Torrisi, L., Bitner-Gregersen, E., Serio, M., and Onorato, M.: Rogue waves in crossing seas: the Louis Majesty accident, J. Geophys. Res., 117, C00J10, doi:10.1029/2012JC007923, 2012.

Cherneva, Z., Tayfun, M. A., and Guedes Soares, C.: Statistics of nonlinear waves generated in an offshore wave basin, J. Geophys. Res., 114, C08005, doi:10.1029/2009JC005332, 2009.

Dean, R.: Abnormal waves: a possible explanation, in: Water Wave Kinematics, edited by: Torum, A. and Gudmestat, O., Kluwer, Amsterdam, 609–612, 1990.

Ewans, K. C., Bitner-Gregersen, E., and Guedes Soares, C.: Estimation of wind-sea and swell components in a bimodal sea state, J. Offshore Mech. Arct. Eng., 128, 265–270, 2006.

Fedele, F. and Arena, F.: Weakly-nonlinear statistics of high random waves, Phys. Fluids, 17, 026601, doi:10.1063/1.1831311, 2005.

Fedele, F., Cherneva, Z., Tayfun, M. A., and Guedes Soares, C.: Nonlinear Schrödinger invariants and wave statistics, Phys. Fluids, 22, 036601, doi:10.1063/1.3325585, 2010.

Fonseca, N., Pascoal, R., Guedes Soares, C., Clauss, G. F., and Schmittner, C. E.: Numerical and experimental analysis of extreme wave induced vertical bending moments on a FPSO, Appl. Ocean Res., 32, 374–390, 2010.

Forristall, G.: Wave crest heights and deck damage in hurricanes Ivan, Katrina and Rita, Offshore Technology Conference (OTC), Houston, Texas, 18620-MS, doi:10.4043/18620-MS, 2007.

Goda, Y.: Random Seas and Design of Maritime Structures, Advanced Series on Ocean Engineering, 15, World Scientific, Singapore, 2000.

Gramstad, O. and Trulsen, K.: Influence of crest and group length on the occurrence of freak waves, J. Fluid Mech., 582, 463–472, 2007.

Guedes Soares, C.: Representation of double-peaked sea wave spectra, Ocean Eng., 11, 185–207, 1984.

Guedes Soares, C.: On the occurrence of double peaked wave spectra, Ocean Eng., 18, 167–171, 1991.

Guedes Soares, C. and Carvalho, A. N.: Probability distributions of wave heights and periods in measured combined sea states from the Portuguese coast, J. Offshore Mech. Arct. Eng., 125, 198–204, 2003.

Guedes Soares, C. and Carvalho, A. N.: Probability distributions of wave heights and periods in combined sea-states measured off the Spanish coast, Ocean Eng., 52, 13–21, 2012.

Guedes Soares, C. and Nolasco, M.: Spectral modelling of sea states with multiple wave systems, J. Offshore Mech. Arct. Eng, 114, 278–284, 1992.

Guedes Soares, C., Bitner-Gregersen, E., and Antão, P.: Analysis of the frequency of ship accidents under severe North Atlantic weather conditions, in: Proceedings of the Conference on De-

sign and Operation for Abnormal Conditions II (RINA); London, United Kingdom, London, RINA, 221–230, 2001.

Guedes Soares, C., Fonseca, N., and Pascoal, R.: Abnormal wave induced load effects in ship structures, J. Ship Res., 52, 30–44, 2008.

Guedes Soares, C., Cherneva, Z., Petrova, P. G. and Antão, E.: Large waves in sea states, in: Marine Technology and Engineering, Volume 1, edited by: Guedes Soares, C., Garbatov, Y., Fonseca, N., and Teixeira, A. P., Taylor & Francis Group, London, UK, 79–95, 2011.

Janssen, P.: Nonlinear four-wave interactions and freak waves, J. Phys. Oceanogr., 33, 863–884, 2003.

Kharif, C., Pelinovsky, E., and Slunyaev, A.: Rogue Waves in the Ocean, Springer-Verlag Berlin Heidelberg, Germany, 2009.

Longuet-Higgins, M.: On the statistical distribution of the heights of sea waves, J. Mar. Res., 11, 245–266, 1952.

Longuet-Higgins, M.: The effect of nonlinearities on statistical distributions in the theory of sea waves, J. Fluid Mech., 17, 459–480, 1963.

Longuet-Higgins, M.: On the joint distribution of the periods and amplitudes of sea waves, J. Geophys. Res., 80, 2688–2694, 1975.

Longuet-Higgins, M.: On the joint distribution of wave periods and amplitudes in a random wave field, P. R. Soc. A, 389, 241–258, 1983.

Lucas, C., Boukhanovsky, A., and Guedes Soares, C.: Modelling the climatic variability of directional wave spectra, Ocean Eng., 38, 1283–1290, 2011.

Mori, N. and Janssen, P.: On kurtosis and occurrence probability of freak waves, J. Phys. Oceanogr., 36, 1471–1483, 2006.

Mori, N. and Yasuda, T.: Effects of high order nonlinear interactions on unidirectional wave trains, Ocean Eng., 29, 1233–1245, 2002.

Mori, N., Onorato, M, Janssen, P., Osborne, A. R., and Serio, M.: On the extreme statistics of long-crested deep water waves: Theory and experiments, J. Geophys. Res., 112, C09011, doi:10.1029/2006JC004024, 2007.

Onorato, M. and Proment, D.: Nonlinear interactions and extreme waves: Envelope equations, in: Marine Technology and Engineering, Volume 1, edited by: Guedes Soares, C., Garbatov, Y., Fonseca, N., and Teixeira, A. P., Taylor & Francis Group, London, UK, 135–146, 2011.

Onorato, M., Osborne, A. R., Serio, M., and Bertone, S.: Freak waves in random oceanic sea states, Phys. Rev. Lett., 86, 5831, doi:10.1103/PhysRevLett.86.5831, 2001.

Onorato, M., Osborne, A. R., and Serio, M.: Extreme wave events in directional, random oceanic sea states, Phys. Fluids, 14, 25–28, 2002.

Onorato, M., Osborne, A. R., Serio, M., Cavaleri, L., Brandini, C., and Stansberg, C.: Observation of strongly non-Gaussian statistics for random sea surface gravity waves in wave flume experiments, Phys. Rev. Lett. E, 70, 067302, doi:10.1103/PhysRevE.70.067302, 2004.

Onorato, M., Osborne, A. R., and Serio, M.: On deviations from Gaussian statistics for surface gravity waves, in: Proceedings of the 14th "Aha Huliko" Winter Workshop, Hawaii, 79–83, 2005.

Onorato, M., Osborne, A. R., and Serio, M.: Modulational instability in crossing sea states: a possible mechanism for the formation of freak waves, Phys. Rev. Lett., 96, 014503, doi:10.1103/PhysRevLett.112.068103, 2006a.

Onorato, M., Osborne, A. R., Serio, M., Cavaleri, L., Brandini, C., and Stansberg, C.: Extreme waves, modulational instability and second order theory: wave flume experiments on irregular waves, Eur. J. Mech. B-Fluid, 25, 586–601, 2006b.

Onorato, M., Waseda, T., Toffoli, A., Cavaleri, L., Gramstad, O., Janssen, P., Kinoshita, T., Monbaliu, J., Mori, N., Osborne, A. R., Serio, M., Stansberg, C., Tamura, H., and Trulsen, K.: Statistical properties of directional ocean waves: The role of the modulational instability in the formation of extreme events, Phys. Rev. Lett., 102, 114502, doi:10.1103/PhysRevLett.102.114502, 2009.

Onorato, M., Proment, D., and Toffoli, A., Freak waves in crossing seas, Eur. Phys. J.-Spec. Top., 185, 45–55, doi:10.1140/epjst/e2010-01237-8, 2010.

Petrova, P. and Guedes Soares, C.: Probability distributions of wave heights in bimodal seas in an offshore basin, Appl. Ocean Res., 31, 90–100, 2009.

Petrova, P. and Guedes Soares, C.: Wave height distributions in bimodal sea states from offshore basins, Ocean Eng., 38, 658–672, doi:10.1016/j.oceaneng.2010.12.018, 2011.

Petrova, P., Cherneva, Z., and Guedes Soares, C.: On the adequacy of second-order models to predict abnormal waves, Ocean Eng., 34, 956–961, 2007.

Petrova, P., Tayfun M. A., and Guedes Soares, C.: The effect of third-order nonlinearities on the statistical distributions of wave heights, crests and troughs in bimodal crossing seas, J. Offshore Mech. Arct. Eng., 135, 021801, doi:10.1115/1.4007381, 2013.

Rice, S.: Mathematical analysis of random noise, Bell Syst. Tech. J., 24, 46–156, 1945.

Rodríguez, G. R. and Guedes Soares, C.: The bivariate distribution of wave heights and periods in mixed sea states, J. Offshore Mech. Arct. Eng., 121, 102–108, 1999.

Rodríguez, G. R., Guedes Soares, C., Pacheco, M. B., and Pérez-Martell, E.: Wave height distribution in mixed sea states, J. Offshore Mech. Arct. Engng., 124, 34-40, 2002.

Shemer, L. and Sergeeva, A.: An experimental study of spatial evolution of statistical parameters in a unidirectional narrow-banded random wave field, J. Geophys. Res., 114, C01015, doi:10.1029/2008JC005077, 2009.

Shukla, P., Kourakis, I., Eliasson, B., Marklund, M., and Stenflo, L.: Instability and evolution of nonlinearly interacting water waves, Phys. Rev. Lett., 97, 094501, doi:10.1103/PhysRevLett.97.094501, 2006.

Socquet-Juglard, H., Dysthe, K., Trulsen, K., Krogstad, H. E., and Liu, J.: Probability distributions of surface gravity waves during spectral changes, J. Fluid Mech., 542, 195–216, 2005.

Tamura, H., Waseda, T., and Miyazawa, Y.: Freakish sea state and swell-wind sea coupling: numerical study of the Suwa-Maru incident, Geophys. Res. Lett., 36, L01607, doi:10.1029/2008GL036280, 2009.

Tayfun, M. A.: Distribution of large wave heights, J. Waterw. Port C-ASCE, 116, 686–707, 1990.

Tayfun, M. A.: Distributions of envelope and phase in weakly nonlinear random waves, J. Eng. Mech.-ASCE, 120, 1009–1025, 1994.

Tayfun, M. A.: Statistics of nonlinear wave crests and groups, Ocean Eng., 33, 1589–1622, 2006.

Tayfun, M. A.: Distribution of wave envelope and phase in wind waves, J. Phys. Oceanogr., 38, 2784–2800, 2008.

Tayfun, M. A.: On the distribution of large wave heights: Nonlinear effects, in: Marine Technology and Engineering, Volume 1, edited by: Guedes Soares, C., Garbatov, Y., Fonseca, N., and Teixeira, A. P., Taylor & Francis Group, London, UK, 247–268, 2011.

Tayfun, M. A. and Fedele, F.: Wave-height distributions and nonlinear effects, Ocean Eng., 34, 1631–1649, 2007.

Tayfun, M. A. and Lo, J.-M.: Nonlinear effects on wave envelope and phase, J. Waterw. Port C-ASCE, 116, 79–100, 1990.

Toffoli, A., Lefevre J., Bitner-Gregersen, E., and Monbaliu, J.: Towards the identification of warning criteria: Analysis of a ship accident database, Appl. Ocean Res., 27, 281–291, 2005.

Toffoli, M., Onorato, M., and Monbaliu, J.: Wave statistics in unimodal and bimodal seas from a second-order model, Eur. J. Mech B-Fluid, 25, 649–661, 2006.

Toffoli, A., Bitner-Gregersen, E., Onorato, M., and Babanin, A.: Wave crest and trough distributions in a broad-banded directional wave field, Ocean Eng., 35, 1784–1792, 2008.

Toffoli, A., Bitner-Gregersen, E., Osborne, A. R., Serio, M., Monbaliu, J., and Onorato, M.: Extreme waves in random crossing seas: Laboratory experiments and numerical simulations, Geophys. Res. Lett., 38, L06605, doi:10.1029/2011GL046827, 2011.

Tomita, H. and Kawamura, T.: Statistical analysis and inference from the in-situ data of the Sea of Japan with relevance to abnormal and/or freak waves, in: Proceedings of the 10th International Offshore and Polar Engineering Conference (ISOPE), Seattle, USA, 28 May–2 June 2000, 116–122, 2000.

Trulsen, K. and Dysthe, K. B.: Freak waves – a three-dimensional wave simulation, in: Proceedings of the 21st Symposium on Naval Hydrodynamics, National Academy Press, Washington, DC, 550–560, 1997.

Waseda, T., Kinoshita, T., and Tamura, H.: Evolution of a random directional wave and freak wave occurence, J. Phys. Oceanogr., 39, 621–639, 2009.

Zhang, H., Cherneva, Z., Guedes Soares, C., and Onorato, M.: Comparison of distributions of wave heights from nonlinear Schroedinger equation simulations and laboratory experiments, in: Proceedings of the 32nd International Conference on Ocean, Offshore and Arctic Engineering, Nantes, France, 9–14 June 2013, OMAE2013-11633, 2013.